High Strain Rate Elasto-Plasticity Identification using the Image-Based Inertial Impact (IBII) Test Part 2: Experimental Validation

Lloyd Fletcher[1] Frances Davis[1] Sarah Dreuilhe[1] Aleksander Marek[1]
Fabrice Pierron[1]
[1]Mechanical Engineering, Faculty of Engineering and Physical Sciences,
University of Southampton, UK

Abstract

Current high strain rate testing techniques typically rely on the split-Hopkinson bar (SHB). The early response in an SHB test is corrupted by inertia making it difficult to accurately characterise the transition from elasticity to plasticity for metals. Therefore, a new test method is required. This article is the second in a two part series which aims at developing a new high strain rate test for elasto-plasticity identification using the Image-Based Inertial Impact (IBII) method. The goal of this article is to validate the new method experimentally using IBII tests on aluminium 6082-T6 (minimal rate sensitivity) and stainless steel 316L (rate sensitive). Comparison of the quasi-static and dynamic stress-strain curves for the aluminium case showed minimal difference providing experimental validation of the method. The same comparison for the steel showed that the method was able to detect rate sensitivity.

1 Introduction

There are many scenarios in industry which subject metals to high strain rate loads for example: machining, forming, blast, crash *etc.* In order to design metallic components to resist impact loads it is important to characterise their response over a range of strain rates. The most common technique for analysing the high strain rate response of metals is the split-Hopkinson bar (SHB) technique [1]. The traditional SHB method relies on the test sample undergoing uni-axial deformation with the sample in a state of quasi-static equilibrium [1, 2]. In the early portion of an SHB test there are stress waves within the sample which violates the assumption of quasi-static equilibrium. This makes it extremely difficult to accurately measure the elastic response of the material and for metals it is difficult to accurately characterise the transition between elasticity and plasticity. This leads to considerable scatter even in data for the high strain rate yield stress of common metal alloys. For example consider the plastic response of 316L stainless steel identified by different authors using the SHB technique as shown in Figure 1. Note that for the first case [3] the data was obtained at 1000 s^{-1} and a Ludwik plasticity law was identified from the data. The remaining data was reconstructed from [4] using the Ludwik hardening and Johnson-Cook rate sensitivity parameters from [5–7]. Here we observe that there is a large amount of scatter between different authors with the initial yield stress being anywhere between 325 MPa and 625 MPa. This leads to considerable uncertainty about the overall strain rate sensitivity even when testing a material that is nominally the same steel alloy.

There is a clear need for a new test method that allows for the characterisation of the transition between elasticity and plasticity for metals to allow for accurate rate sensitivity identification. Recently, new high strain test methods have been developed that leverage advances

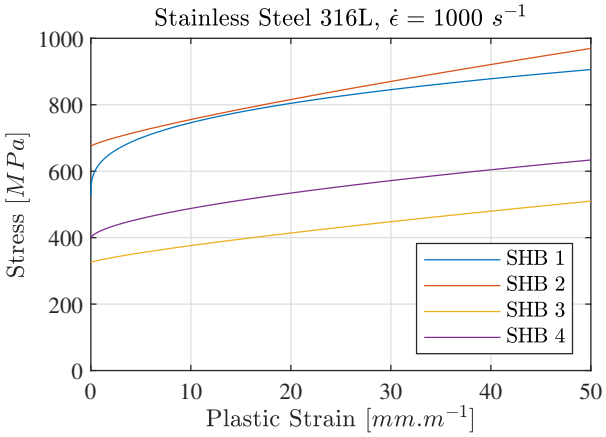

Figure 1: Comparison of the identified plastic response of stainless steel 316L at a strain rate on the order of 1000 s^{-1} using the SHB. Data is taken from the following references: SHB 1 [3]; SHB 2 [6]; SHB 3 [7] and; SHB 4 [5].

in ultra-high speed imaging technology to measure the full-field strains and accelerations. The information is then used to identify material properties using an inverse identification procedure such as the Virtual Fields Method (VFM) [8–14]. One of these new methods is the Image-Based Inertial Impact (IBII) test, which has proven to be an excellent tool for probing the elastic response and tensile failure stress of brittle and quasi-brittle materials [11,12,15,16]. More recently this method was used to investigate the visco-plastic response of titanium [17, 18]. However, in this case the data for the plasticity law was taken from quasi-static tests and only the rate sensitivity parameter of the Johnson-Cook model was identified. Therefore, the purpose of the present series of articles is to develop a new elasto-plasticity identification procedure using the IBII test method.

Part 1 of this series [19] focused on the validation of the Virtual Fields Method (VFM) identification procedure using finite element data and the subsequent analysis of error propagation in the full-field measurement chain using synthetic image deformation (in a similar manner to refs. [20–24]). These image deformation simulations allowed for the rational selection of data processing parameters and prediction of the experimental error bounds. The purpose of the present paper is to apply the developed elasto-plastic identification method to experimental data and then perform a comparison of the experimental data to that predicted by the image deformation simulatiosn presented in part 1. Two materials are considered, aluminium 6082-T6 which is exhibits almost no rate sensitivity [25–27] and stainless steel 316L which has significant rate sensitivity [3, 5–7] (while the magnitude of the rate sensitivity for 316L is uncertain, see Figure 1). Thus, comparison of quasi-static and dynamic test data for aluminium 6082-T6 serves to validate the method and the same comparison for stainless steel 316L demonstrates the ability of the method to discriminate rate sensitivity.

This paper begins by briefly revisiting the VFM theory required to perform the identifications followed by a section which outlines the experimental methodology and set-up. The next section describes the experimental results showing the kinematics for the dynamic tests and comparisons of the stress-strain response between the quasi-static and dynamic cases. Following this a comparison between the experimental data and the synthetic image deformation simulations is performed to analyse the predictive capability of the image deformation procedure. The final sections of this paper discuss the limitations of the method and potential directions for future work before summarising the main conclusions.

2 The Virtual Fields Method

The virtual fields method (VFM) is an inverse identification technique that uses full-field measurement data to identify the constitutive response of materials. The goal here is to apply the VFM to the IBII configuration shown in Figure 2 and develop a method to identify the elasto-plastic response of a metal. The first step of the VFM is to consider the principle of virtual work. For the IBII configuration shown in Figure 2 a number of simplifications are made, 1) the sample is in a state of plane stress, 2) the kinematic fields are uniform through-thickness, 3) the material properties do not vary in space and 4) body forces only come from gravity and are negligible. In this case the principle of virtual work is reduced to two dimensions, as follows:

$$\overbrace{\int_S \boldsymbol{\sigma} : \boldsymbol{\varepsilon}^* \mathrm{d}S}^{W^*_{int}} - \overbrace{\int_l \boldsymbol{T} \cdot \boldsymbol{u}^* \mathrm{d}l}^{W^*_{ext}} + \overbrace{\rho \int_S \boldsymbol{a} \cdot \boldsymbol{u}^* \mathrm{d}S}^{W^*_{acc}} = 0 \tag{1}$$

where S is the two dimensional surface of the sample and l is its perimeter. The stress tensor is given by $\boldsymbol{\sigma}$ and the virtual strain tensor is $\boldsymbol{\varepsilon}^*$ which can be derived from the virtual displacement vector, $\boldsymbol{u^*}$, by: $\varepsilon^*_{ij} = \frac{1}{2}\left(\frac{\partial u^*_i}{\partial j} + \frac{\partial u^*_j}{\partial i}\right)$, $i, j = x, y$. The traction vector is denoted $\boldsymbol{T}$ while ρ is the density of the material and $\boldsymbol{a}$ is the acceleration vector. The dot product between vectors is denoted '$\cdot$' and the double dot product between second order tensors is denoted ':'. The principle of virtual work is the weak form of the equilibrium equation and is composed of the internal virtual work W^*_{int}, the virtual work of externally applied forces W^*_{ext} and the virtual work of acceleration W^*_{acc}.

In order to use equation 1 to identify a material model two additional pieces of information are required: the first is a constitutive law which can be substituted for the stress tensor in the internal virtual work term and the second is a set of virtual fields. In the case of linear elasticity equation 1 produces a set of linear equations which are easily solved to identify the relevant material parameters. For non-linear material models, such as elasto-plasticity, equation 1 produces a set of non-linear equations. To solve this set of non-linear equations, a cost function representing the sum of the internal, external, and inertial virtual work is constructed:

$$C_f(\mathbf{K}) = \sum_{t=t_0}^{t_f} \left(\int_S \boldsymbol{\sigma}\left(\boldsymbol{\varepsilon}, \mathbf{K}\right) : \boldsymbol{\varepsilon}^* \, \mathrm{d}S - \int_l \boldsymbol{T} \cdot \boldsymbol{u^*} \mathrm{d}l + \int_S \rho \, \boldsymbol{a} \cdot \boldsymbol{u^*} \, \mathrm{d}S \right)^2 . \tag{2}$$

where the summation is performed over a given set of time steps t from the first frame considered at t_0 to the final frame t_f. The cost function is minimised by updating the constitutive model parameters $\mathbf{K}$, noting that for each iteration the stress must be calculated from the strains measured during the test. Note that for the case of elasto-plasticity, there is no explicit relationship between the measured strain and the stress, therefore the stress components can only be calculated using an iterative stress reconstruction algorithm which separates the strain into its elastic and plastic contributions. The following sections describe the constitutive models and virtual fields that are used with the cost function defined above.

2.1 Constitutive Models

In this work the analysis is limited to the case of isotropic plasticity so a von Mises yield criterion is used. The first hardening law that is considered in this work is a simple linear hardening model. For this case the updated yield stress σ_y is given by:

$$\sigma_y = \sigma_0 + H\epsilon_p \tag{3}$$

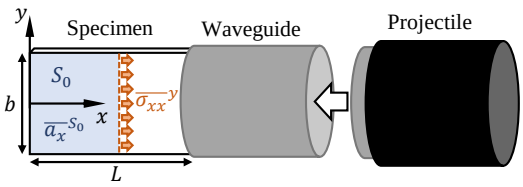

Figure 2: Schematic of the IBII test configuration showing the main tests components.

where σ_0 is the initial yield stress, ϵ_p is the equivalent plastic strain and H is the hardening modulus. For the remainder of this article identifications relating to a linear hardening law are denoted 'LH'.

For most ductile metals the linear hardening law does not accurately describe the smooth transition between elasticity and plasticity. Therefore, a Voce hardening law is also considered, as follows:

$$\sigma_y = \sigma_0 + R_{inf}(1 - exp(-b\epsilon_p)) + R_0\epsilon_p \tag{4}$$

where σ_0 is the initial yield stress and R_0 is the long term hardening modulus. The additional parameters R_{inf} and b describe the curved transition region from the initial yield stress to the long term hardening modulus. For the Voce hardening model there is significant interaction between the σ_0 and R_{inf} parameters so it is more useful to analyse the sum of these two parameters. Here we define the effective yield stress as $\sigma_{YS} = \sigma_0 + R_{inf}$. The Voce hardening law will be denoted with the use of the shorthand 'VH' in subsequent sections of this article.

2.2 Selection of Virtual Fields

Stress-gauge (SG) virtual field: Here we begin with the schematic of IBII test configuration given in Figure 2. Consider a simple virtual field describing a rigid body translation in the x direction, as follows:

$$\begin{cases} u_x^* = 1 \\ u_y^* = 0 \end{cases} \quad \begin{cases} \epsilon_{xx}^* = 0 \\ \epsilon_{yy}^* = 0 \\ \epsilon_{xy}^* = 0 \end{cases} \tag{5}$$

As this virtual field has zero virtual strain substituting this into the principle of virtual work (equation 1) cancels the contribution of the internal virtual work term, W_{int}^*, leaving:

$$\int_l \sigma_{xx} \mathrm{d}l = \rho \int_S a_x \mathrm{d}S \tag{6}$$

When using typical camera-based deformation measurements (*e.g.* digital image correlation or the grid method) the data is obtained on a regular grid of points each with equivalent 'pixel' areas. In this case, the continuous integrals in equation 6 can be approximated as discrete sums (using the rectangle method of numerical integration as described in [9, 16]). Thus, the integral terms of equation 6 become spatial averages as follows:

$$\overline{\sigma_{xx}}^{y} = \rho x \overline{a_x}^{S_0} \tag{7}$$

where $\overline{\sigma_{xx}}^{y}$ is the average stress over the axial section at position x from the free edge of the sample (the red dashed line in Figure 2). Throughout the rest of the article the overline notation coupled with a superscript y is used to indicate a spatial average over an axial section of the

sample. The term $\overline{a_x}^{S_0}$ denotes the surface average of the acceleration over the area S_0 which is taken from the free edge to position x (shown as the blue shaded area in Figure 2). For the remainder of this article the use of the overline notation coupled with a superscript S_0 indicates a spatial average from the free edge to a given axial section. In previous work this equation has been designated the 'stress-gauge' as it allows for the calculation of the average stress at each section of the sample where the density acts as a kind of load-cell calibration factor.

The stress-gauge virtual field is used to build a cost function for non-linear material model identification as follows:

$$C_f^{SG}(\mathbf{K}) = \sum_{x=x_0}^{x_n} \sum_{t=t_0}^{t_f} \left(\overline{\sigma_{xx}\left(\mathbf{K}, \boldsymbol{\varepsilon}\right)}^{y} - \rho x \overline{a_x}^{S_0} \right)^2 \tag{8}$$

where the summation is considered over a given number of time steps t and a given number of axial sections x (from the free edge at x_0 to the furthermost section x_n). This equation can be understood simply as the difference between the average axial stress calculated using the material parameters and the strain and the average stress calculated from the acceleration as given by equation 7. In later sections of this article identifications performed with the stress-gauge virtual field are referred to using the abbreviation 'SG'.

Sensitivity-based (SB) virtual fields: The sensitivity-based virtual fields procedure was developed as a way of automatically selecting virtual fields based on the stress sensitivity maps obtained by perturbing material parameters [28]. The stress sensitivity $\delta\boldsymbol{\sigma}$ is defined as:

$$\delta\boldsymbol{\sigma}^{(i)}\left(\boldsymbol{\varepsilon}, \boldsymbol{K}, t\right) = \boldsymbol{\sigma}\left(\boldsymbol{\varepsilon}, \boldsymbol{K}, t\right) - \boldsymbol{\sigma}\left(\boldsymbol{\varepsilon}, \boldsymbol{K} + \delta K_i, t\right) \tag{9}$$

where $\boldsymbol{K}$ is the vector of model parameters, i denotes the i^{th} model parameter in vector $\boldsymbol{K}$, δK_i is a small perturbation to the model parameter K_i, and t is the time step. The stress sensitivity field naturally highlights areas where a given model parameter is strongly activated. If a small change in the model parameter causes a large change in the stress in a given area then this area encodes more information about that parameter. A stress sensitivity map is generated for each model parameter giving individually tailored virtual fields.

The sensitivity-based virtual fields are used to build a cost function for material parameter identification as follows:

$$C_f^{SB}(\mathbf{K}) = \sum_{i=1}^{n} \frac{1}{\left(\alpha^{(i)}\right)^2} \left[\sum_{t=t_0}^{t_f} \left(\overline{\boldsymbol{\sigma}\left(\boldsymbol{\varepsilon}, \boldsymbol{K}\right) : \boldsymbol{\varepsilon}^{*(i)}}^{S} - \rho\, \overline{\boldsymbol{a} \cdot \boldsymbol{u}^{*(i)}}^{S} \right)^2 \right] . \tag{10}$$

where n is the number of model parameters in $\boldsymbol{K}$ and $\alpha^{(i)}$ is a weight to ensure that each parameter has approximately the same contribution to the cost function. The weight, $\alpha^{(i)}$, is the mean of the m highest internal virtual work W_{int}^{*} values. In this case the overline notation coupled with superscript 'S' is used to indicate a spatial average over the whole surface of the sample. However, it is possible to restrict the surface over which the cost function is calculated by applying virtual boundary conditions that eliminate the contribution of unknown forces on the boundaries of the sample as described in the first part of this series. Additionally, the sensitivity based virtual fields were formulated using the total stress sensitivity as described in [28]. Full details on the implementation of these sensitivity-based virtual fields can be found in ref. [28]. In later sections of this article the sensitivity-based virtual fields are referred to using the abbreviation 'SB'.

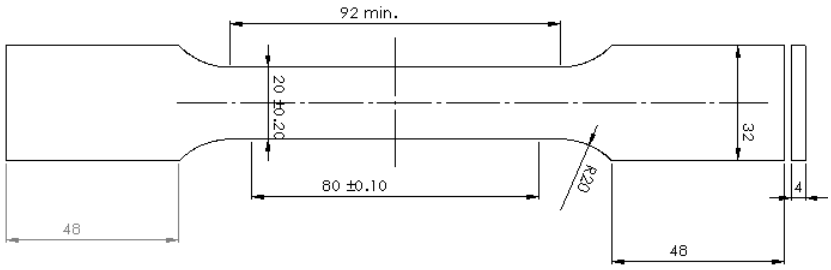

Figure 3: Geometry of dogbone samples used for the quasi-static tests, all dimensions are given in mm.

3 Experimental Method

3.1 Materials and Quasi-Static Testing

Two materials were tested: aluminium 6082-T6 and stainless steel 316L. Quasi-static uni-axial tension tests were performed to characterise the mechanical properties. For each material, 3 dog bone specimens were water-jet cut from 4 mm thick plates. The geometry for the quasi-static test specimens is shown in Figure 3. Note that because the 316L steel exhibits mild anisotropy, all of the steel specimens were cut along the same direction from a single sheet. All tests were conducted using an electromechanical test machine equipped with a 50 kN load cell. Each specimen was loaded in displacement control at 6 $mm.min^{-1}$ until failure occurred. The strain was measured using 0/45/90 strain gauge rosettes in a back-to-back configuration. Note that the strain was averaged over both sides to eliminate the contribution of bending. In later sections of this article the quasi-static test data is compared to the high strain rate data obtained with the IBII test. Therefore, the quasi-static data is referred to using the shorthand 'QS'.

3.2 Image-Based Inertial Impact Test Setup

The IBII tests were conducted in general accordance with the procedures outlined in [29] so only the main details are recalled here. All IBII tests were performed using a purpose-built impact rig at the University of Southampton. An annotated photograph of the main test components is shown in Figure 4. The rectangular test sample was bonded to the rear face of the waveguide using cyanoacrylate glue. The waveguide was then positioned on a wedge shaped foam stand which was placed on a mounting tray aligned to the exit of the barrel.

The projectile and waveguide were cylindrical with a diameter of 45 mm and length of 72 mm. These components were machined from aluminium 7075-T6. The projectile was encased in a Delrin sabot which was used to reduce friction with the barrel of the gas gun. The gas gun chamber pressure was set to achieve a nominal impact speed of 50 $m.s^{-1}$. The actual impact speed was measured for each sample using the light gates at the end of the barrel. The overall average impact speed was 51.0 ± 1.6 $m.s^{-1}$, where the number after the $\pm$ symbol is the standard deviation over all shots.

The rectangular IBII specimens were waterjet cut with nominal dimensions of $70 \times 44 \times 4$ mm. A total of 6 specimens were cut from each material. In order to follow the plastic deformation of the sample a thin layer of white rubber paint (Rustoleum Peel-Coat) was applied to the surface of the samples. A grid pattern was then printed directly onto the white rubber paint layer using the procedure described in [11, 29]. In subsequent sections of this article IBII specimens made from aluminium 6082-T6 are referred to using the shorthand 'Al' while the stainless steel 316L samples use the notation 'St'. Thus, 'Al6' refers to aluminium IBII specimen number six.

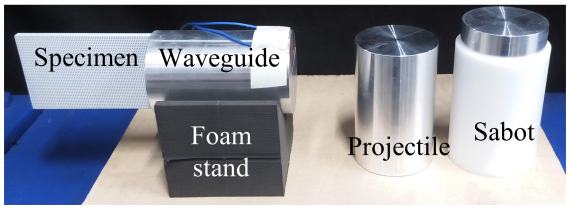

(a)

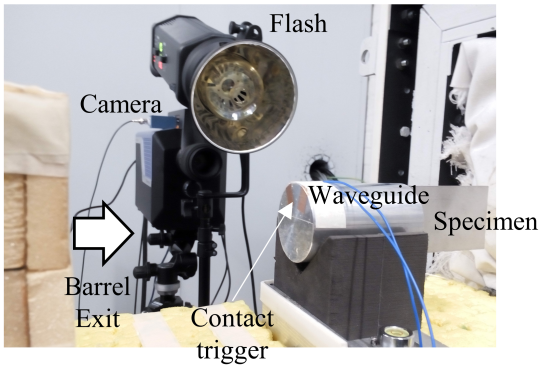

(b)

Figure 4: Photograph of the main test components (a) and experimental set-up showing the imaging system (b).

3.3 Imaging Set-up and Full-Field Measurements

The stress-wave propagation in the samples was imaged using a Shimadzu HPV-X ultra-high speed camera with lighting provided by a Bowens Gemini 1000Pro flash (as shown in Figure 4 (b)). The camera was triggered using a copper contact trigger on the front of the waveguide and the flash was triggered using the light gates at the end of the gas gun barrel. Further details on triggering and synchronisation can be found in ref. [29]. The remaining imaging parameters are summarised in Table 1.

The grid method has been chosen in preference to digital image correlation (DIC) for previous studies using the IBII methodology as it offers an improved trade-off between spatial and measurement resolution [30]. This trade-off is important as the ultra-high speed camera used to make the measurements has a low pixel count. It would be an interesting future study to compare the application of the grid method and DIC for the elasto-plasticity identification procedure presented here using synthetic image deformation as described in part 1 of this series. However, this is beyond the scope of the present work. A detailed description of the grid method theory is not given here but it can be found in the review article in ref. [31]. The key parameters for the grid method analysis are summarised in Table 1 noting that the iterative displacement calculation procedure was used as described in [31].

The general experimental procedure followed that outlined in ref. [29] where the camera was initially aligned to the grid and the sampling was verified using a set of static reference images. An out of plane movement test was then performed to assess the quality of the set-up and ensure that the grid image was slightly blurred to suppress harmonics in the grid method processing.

3.4 Data Processing

All data processing was performed using Matlab (R2018a). The data processing procedure was developed and validated in the first article of this two part series so only the main steps of the

Camera	Shimadzu HPV-X
Pixel Array Size	400×250
Dynamic Range	10 $bits$
Frame Rate	5 $Mfps$
Integration (Shutter) Time	110 ns
Total Images	128
Lens	Sigma 105 mm
Field of View (FOV)	72×45 mm
Measurement Technique	Grid Method
Grid Pitch	0.9 mm
Grid Sampling ($pxpp$)	5 $pixels/period$
Window Type	Bi-triangular
Window Width	$2pxpp - 1$
Displacement Calculation	Iterative [31]
Spatial Smoothing	Gaussian
Temporal Smoothing	Savitsky-Golay

Table 1: Imaging system and full-field measurement parameters. Note that the optimal smoothing kernel sizes are different for the different identification methods so the kernel sizes are not specified here.

procedure are recalled here. The reader is referred to the flow chart appearing in Figure 6 of part 1 [19] as an overview of the data processing procedure.

The first step is to extract the displacement fields from the raw images using the grid method. This was implemented using the grid method code which was made available as part of [31] and can be freely downloaded here[1]. The displacement fields are then temporally smoothed using a 2nd order Savitsky-Golay filter using the Matlab function *'sgolayfilt'*. The size of the temporal smoothing kernel, T_{ks}, was specified as an odd number of frames. From the temporally smoothed displacement fields the acceleration fields are calculated by applying a central finite difference method twice, once to obtain velocity and again to obtain acceleration. All differentiations were performed using the Matlab function *'gradient'*. The temporally smoothed displacements where then smoothed in space with a Gaussian filter using the Matlab function *'imgaussfilt'*. The size of the spatial smoothing kernel, S_{ks}, was specified as an odd integer number of pixels. The standard deviation of the filter was then set based on: $S_{ks} = 2\lceil 2SD \rceil + 1$ where SD is the standard deviation of the Gaussian filter and $\lceil\rceil$ is the ceiling function. After spatially smoothing the displacements the strain fields were calculated using a centred finite difference algorithm. The smoothing kernel sizes used for each identification procedure and constitutive model are summarised in Table 2. These parameters were chosen based on the image deformation parameter sweep performed in part 1 [19]. For all full-field measurement techniques data is lost on the edges of the sample; when using the grid method one grid pitch of data is lost at the sample edges. This data was reconstructed here using a simple padding procedure.

Having obtained the acceleration and strain fields they are used in the inverse identification procedure described in Section 2 to obtain the elasto-plastic material parameters. Identifications based on either the SG or the SB virtual fields cost function require that the stress is calculated from the strains using the constitutive parameters. This was achieved using a return mapping algorithm (RMA) which was developed based on the work of [32] and validated in part 1 of this series (the code is also provided as part of the attached digital dataset).

[1] http://www.thegridmethod.net/code

Material	Plasticity Model	Virtual Field	T_{ks} $[frames]$	S_{ks} $[pixels]$
Aluminium	Linear	SG	15	31
Aluminium	Linear	SB	15	51
Aluminium	Voce	SG	15	31
Aluminium	Voce	SB	31	51
Steel	Linear	SG	21	31
Steel	Linear	SB	11	51
Steel	Voce	SG	31	31
Steel	Voce	SB	15	51

Table 2: Optimal smoothing parameters from the image deformation analysis performed in part 1 [19].

The use of spatial and temporal smoothing leads to edge artefacts in the kinematic fields. If this corrupted data is included in the inverse identification it leads to erroneous results. Fortunately it is possible to exclude most of the corrupted data from the cost function for either the SG or the SB virtual fields. For the SG virtual field a minimum of $2pxpp+1$ axial slices were excluded from both edges of the sample where $pxpp$ is the grid sampling. If a large amount of smoothing was applied then data was excluded based on the following rule: $\lceil S_{ks}/2 \rceil + pxpp + 1$. This rule was only applied if it resulted in a larger data exclusion than $2pxpp + 1$. The virtual mesh of the SB virtual fields was set to be 14×14 elements with the virtual boundary conditions on all edges of the sample being fixed. Fixing the edge boundary conditions for the SB virtual fields allows data to be excluded from all edges of the sample. Therefore, the SB virtual fields used the same spatial data exclusion rule as for the SG virtual field but data was excluded from all edges of the sample. For both the SG and SB virtual fields a minimum number of frames equal to $\lceil T_{ks} \rceil + 6$ were excluded from the end of the data to remove temporal edge effect coming from differentiation and from the smoothing filter. Furthermore, due to differences in triggering times between samples additional frames were excluded from the end of the data to remove any unloading that occurred in the sample.

As was shown in part 1 of this series, down-sampling the data by including every third frame in the cost function was found to have a minimal effect on the systematic error of the identification. Down-sampling the data also increases the strain increment for the RMA and decreases overall computation time. Therefore, all data was down-sampled by taking every third frame before being input into the either the SG or the SB virtual fields cost function. Note that the intermediate frames still contribute through the temporal smoothing and temporal differentiation procedures. Finally, the same non-linear optimisation algorithms as described in part 1 were used for each case [14]. Three random starting points were generated within $\pm 30\%$ of the predicted response using the quasi-static data. The identified parameters were taken as those returning the overall minimum value of the cost function. The Matlab code used to calculate the kinematic fields from the experimental images and to perform the inverse identification is provided in the digital dataset detailed at the end of this article.

3.5 Measurement Resolution

The raw displacement resolution was calculated for each specimen by taking a series of 128 static images prior to the IBII test. These images were processed using the same procedure as for the dynamic test to obtain the displacement fields and then smoothed/differentiated to obtain the strain/acceleration fields. The noise floor was taken as the standard deviation of

Spec.	Raw Disp. px	Raw Disp. μm	Smooth Disp. μm	Accel. $\times 10^6\ m.s^{-2}$	Strain $mm.m^{-1}$	Strain Inc. $mm.m^{-1}$
Al1	0.0083	1.50	0.26	1.53	0.12	0.032
Al2	0.0092	1.66	0.30	1.69	0.13	0.035
Al3	0.0088	1.59	0.27	1.62	0.13	0.033
Al4	0.0097	1.75	0.27	1.65	0.13	0.034
Al5	0.0092	1.65	0.28	1.70	0.14	0.035
Al6	0.0095	1.72	0.29	1.77	0.13	0.037
St1	0.0086	1.55	0.25	1.22	0.10	0.021
St2	0.0097	1.75	0.31	1.37	0.12	0.024
St3	0.0103	1.86	0.30	1.47	0.12	0.025
St4	0.0094	1.70	0.31	1.34	0.13	0.023
St5	0.0100	1.80	0.29	1.42	0.12	0.025
St6	0.0097	1.75	0.30	1.38	0.13	0.024
ID	0.0087	1.56	0.26	1.43	0.12	0.027

Table 3: Measurement resolutions for all IBII specimens tested. Note that the smoothed and derived quantities are taken as averages over all four cases, see Table 2 (linear or voce hardening, SG or SB virtual fields). The image deformation (ID) resolutions are provided for comparison.

the resulting noise maps. The resulting measurement resolutions are summarised in Table 3. Given that each combination of virtual field and hardening law requires a different combination of optimal smoothing parameters the measurement resolution for derived quantities (*i.e.* strain and acceleration) is different for each case. Therefore the measurement resolutions for the derived quantities given in Table 3 are averaged over all four cases (combination of linear/voce hardening and SG/SB virtual fields) for each specimen. The measurement resolution for each specific case is given in the attached digital dataset along with the Matlab code and static images used to perform the calculations.

4 Experimental Results

4.1 Dynamic Kinematic Fields

A sequence of kinematic fields for the specimen Al1 is given in Figure 5. In this figure the optimal smoothing parameters for the identification with the SG virtual field are used (see Table 2). Similarly, a sequence of kinematic fields for the steel specimen St1 are shown in Figure 6 using the optimal smoothing parameters for the SG virtual field.

The displacement fields for both materials show an increase in mean intensity which is consistent with the rigid translation of the sample after impact. Analysis of the kinematics also shows that the fields are mostly symmetric in the vertical direction. The elastic wave is clearly evident in the acceleration fields for both samples as a front of negative acceleration with a peak magnitude on the order of $10^6\ m.s^{-2}$. The deformation is predominantly axial (in the direction of impact) and concentrated near the impact edge. This is visible as a large build up of strain at the right hand edge where most of the plastic deformation occurs. Both materials have peak total strain values on the order of 3%. Finally, the total strain rate fields for both metals show peak values on the order of $10^3\ s^{-1}$ in compression.

As can be seen in Figures 5 and 6 the strain rate field is heterogeneous. This is advantageous as it may be possible to obtain some strain rate sensitivity information by combining the methodology presented in this work with that in [17, 18]. However, this is beyond the scope of

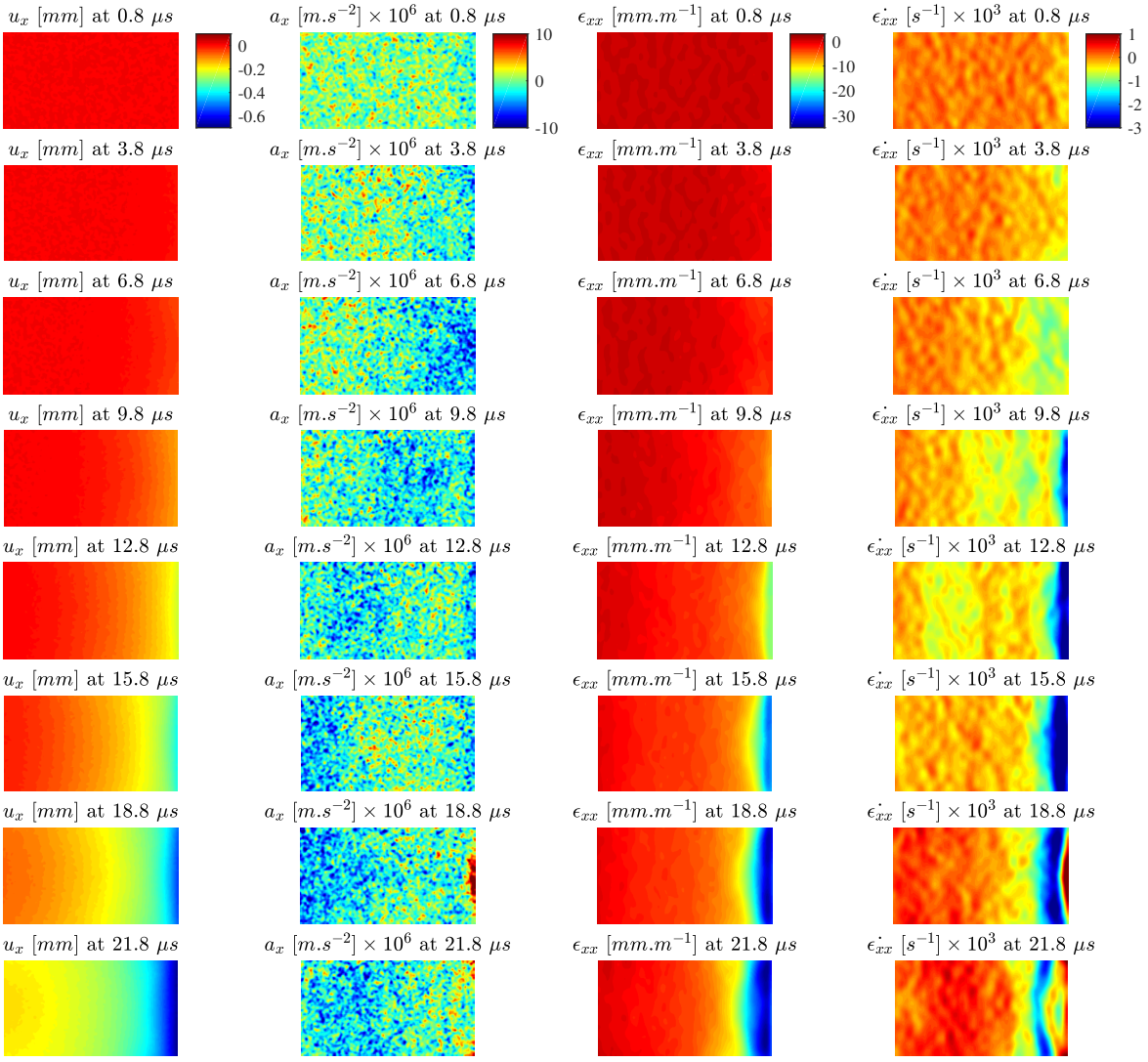

Figure 5: Axial kinematic fields for the aluminium specimen Al1 using the optimal smoothing kernels for the SG virtual field (see Table 2).

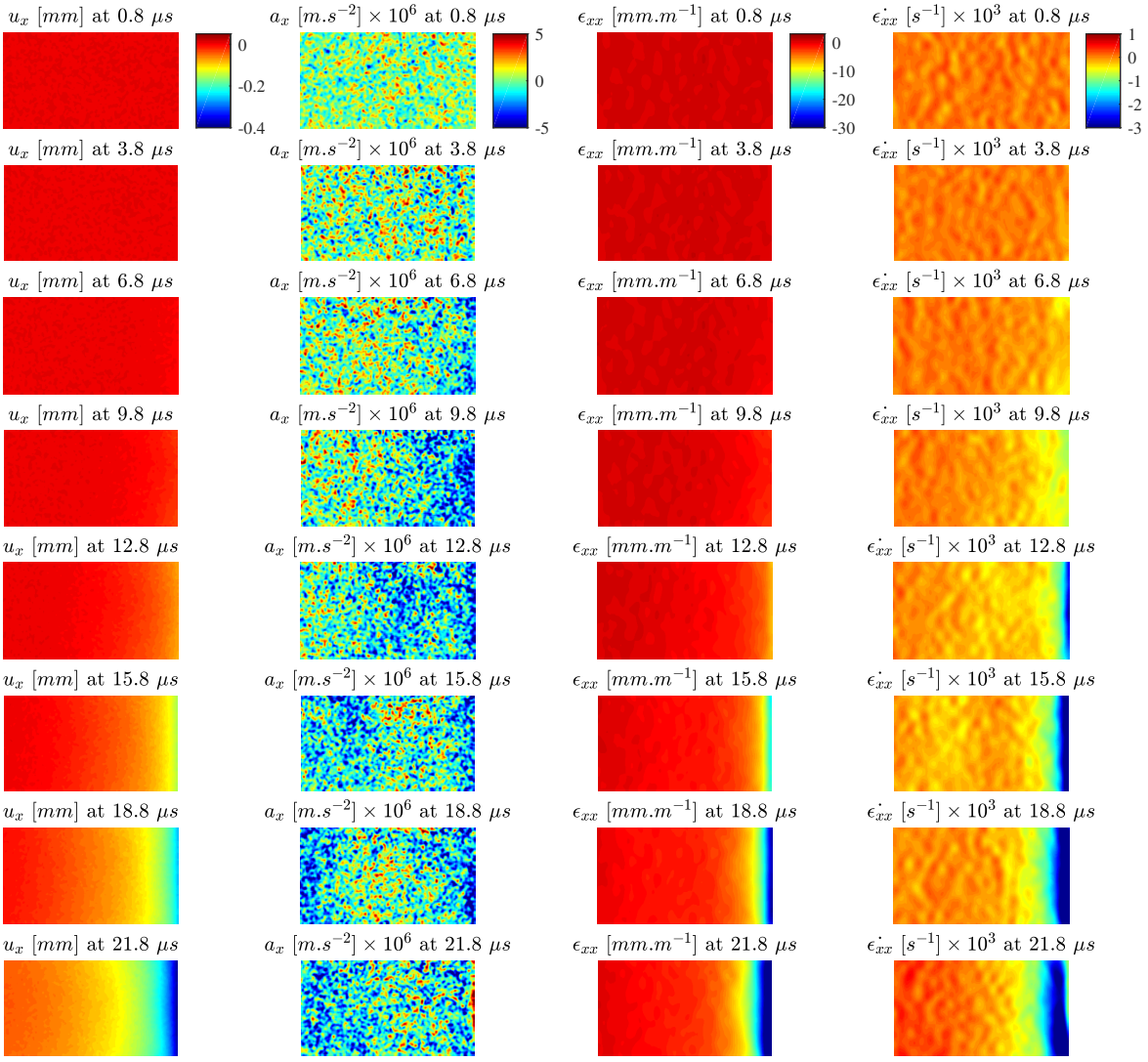

Figure 6: Axial kinematic fields for the steel specimen St1 using the optimal smoothing kernels for the SG virtual field (see Table 2).

Spec.	$\hat{\dot{\epsilon}}_{xx}$ $[s^{-1}]$	Spec.	$\hat{\dot{\epsilon}}_{xx}$ $[s^{-1}]$
Al1	-973	St1	-1414
Al2	-857	St2	-1542
Al3	-968	St3	-1116
Al4	-857	St4	-1174
Al5	-959	St5	-1417
Al6	-822	St6	-1376

Table 4: Effective strain rate for all IBII specimens.

the present work. In order to have a comparative measure of the strain rate for this type of heterogeneous test we define an effective strain rate as follows:

$$\hat{\dot{\epsilon}}_{ij} = \frac{\sum^N \sum^t \epsilon_{ij} \dot{\epsilon}_{ij}}{\sum^N \sum^t \epsilon_{ij}} \quad , \quad i,j = x,y \tag{11}$$

where the summations are performed over all spatial measurement points N and all time steps t. Note that the data exclusion rules described in Section 3.4 are applied during the calculation of the effective strain rate to avoid smoothing edge effects biasing the results. This measure of strain rate provides most weight to points experiencing high strains and mitigates the contribution of points with low strains. The strain and strain rate terms in equation 11 can be substituted for any strain component of interest. For the standard rectangular IBII samples used in this work the deformation is mostly axial so $\hat{\dot{\epsilon}}_{xx}$ is most relevant. The effective axial strain rate for all tested samples is summarised in Table 4. This data shows that the effective strain rate is consistent between specimens for the different materials considered with the steel exhibiting a slightly higher strain rate. Both materials experience an effective strain rate on the order of 1000 s^{-1}.

Given that the focus of this work is elasto-plasticity identification the plastic strain rate is also of interest. The effective plastic strain rate $\hat{\dot{\epsilon}}_p$ can be calculated by replacing the strain and strain rate terms in equation 11 with the equivalent plastic strain ϵ_p and equivalent plastic strain rate $\dot{\epsilon}_p$. The calculation of the plastic strain and strain rate requires knowledge of the constitutive parameters to partition the total strain into elastic and plastic components. This is discussed in the next section along with the results of the inverse identification.

4.2 Dynamic Identification: Aluminium

The results of the inverse identification procedure for all aluminium IBII samples are given in Table 5. Here we begin the analysis with the linear hardening case. The results for the initial yield stress have a remarkably low coefficient of variation (COV) for both identification methods (about 1%). The median initial yield stress over all samples is also consistent between identification methods with the result for the SG and SB virtual fields being within one median absolute deviation (MAD) of each other. The COV for the identified hardening modulus is higher for both identification methods which is expected as this parameter is more difficult to identify. The mean hardening modulus over all samples is lower for SB virtual fields and when comparing the hardening modulus for each individual sample the result is always lower for the SB virtual fields. Another difference between identification methods is that the predicted peak plastic strain is higher for the SG virtual field which would seem counter intuitive considering that the hardening modulus is lower for the SB virtual fields. The reason for this results from the smoothing parameters selected for each method (see Table 1), where the SB virtual fields

	Linear				Voce						
SG	σ_0 $[MPa]$	H $[MPa]$	$max(\epsilon_p)$ [%]	$\hat{\dot{\epsilon}_p}$ $[s^{-1}]$	σ_0 $[MPa]$	R_0 $[MPa]$	R_{inf} $[MPa]$	b $[-]$	σ_{YS} $[MPa]$	$max(\epsilon_p)$ [%]	$\hat{\dot{\epsilon}_p}$ $[s^{-1}]$
Al1	275	1885	3.31	1523	0	1423	281	7224	281	3.33	1476
Al2	279	2225	3.16	1307	0	1627	285	6958	285	3.18	1264
Al3	281	1862	3.44	1764	0	1293	287	6984	287	3.46	1646
Al4	284	1452	3.97	1322	218	1055	72	4428	290	3.98	1321
Al5	280	2077	3.08	1607	0	1501	286	6111	286	3.10	1527
Al6	274	1923	3.80	1454	130	1580	148	8070	278	3.82	1438
Median	279	1904	3.38	1488	-	1462	-	6971	286	3.40	1457
MAD	2.9	107	0.26	143	-	142	-	556	2.2	0.26	103
COV %	1.0	5.6	7.6	9.6	-	9.7	-	8.0	0.8	7.6	7.1
SB	σ_0 $[MPa]$	H $[MPa]$	$max(\epsilon_p)$ [%]	$\hat{\dot{\epsilon}_p}$ $[s^{-1}]$	σ_0 $[MPa]$	R_0 $[MPa]$	R_{inf} $[MPa]$	b $[-]$	σ_{YS} $[MPa]$	$max(\epsilon_p)$ [%]	$\hat{\dot{\epsilon}_p}$ $[s^{-1}]$
Al1	282	893	3.00	1448	0	716	269	4606	269	2.98	1481
Al2	287	1037	2.74	1211	0	743	283	6863	284	2.73	1314
Al3	280	1021	2.56	1553	0	791	274	4998	274	2.28	1330
Al4	288	572	3.53	1245	226	591	62	3344	289	3.50	1402
Al5	278	1040	2.79	1484	14	643	259	5426	273	2.66	1443
Al6	278	1110	3.31	1389	11	1118	259	7254	269	3.07	1363
Median	281	1029	2.89	1418	-	729	-	5212	274	2.85	1383
MAD	2.9	46	0.24	100	-	74	-	1129	4.4	0.20	57
COV %	1.0	4.5	8.3	7.0	-	10.1	-	21.7	1.6	7.2	4.1

Table 5: Identified elasto-plastic parameters from the dynamic tests on aluminium 6082-T6 samples. Note that the coefficient of variation (COV) is taken as the ratio of the median absolute deviation (MAD) to the median.

required a larger spatial smoothing kernel leading to larger region of data being excluded from the impact edge where the plastic strain concentrates (see Figure 5). However, the effective plastic strain rate for all samples is quite consistent and typically on the order of 1400 s^{-1}.

Next we consider the identification of the Voce model on experimental data. The most obvious observation for both identification methods is the interaction between the σ_0 and R_{inf} parameters. However, analysis of the effective yield stress (recall $\sigma_{YS} = \sigma_0 + R_{inf}$) shows a low COV for both identification methods with the COV for the SB virtual fields being higher than the SG virtual field. Additionally, the SB virtual fields return a lower effective yield stress than the SG virtual field. The long term hardening modulus, R_0, exhibits similar trends to the hardening modulus for the linear hardening case with the SB virtual fields having a higher COV and giving a lower value for each individual specimen. The curvature parameter b is consistent for both identification methods given that an order of magnitude change in this parameter is required to alter the stress-strain curve shape. Finally, the peak plastic strain and effective plastic strain rate show the same trends as for the linear hardening case. Having shown that the raw identified material parameters are consistent between cases the IBII data is now compared to the quasi-static data.

Aluminium 6082-T6 shows minimal rate sensitivity [25–27] so the quasi-static response serves as a base line comparison to validate the test method. Figure 7 shows a comparison of the quasi-static stress-strain curves with the identified material models from the dynamic test data. Note that all three quasi-static tests are shown as black lines in Figure 7 as there is minimal

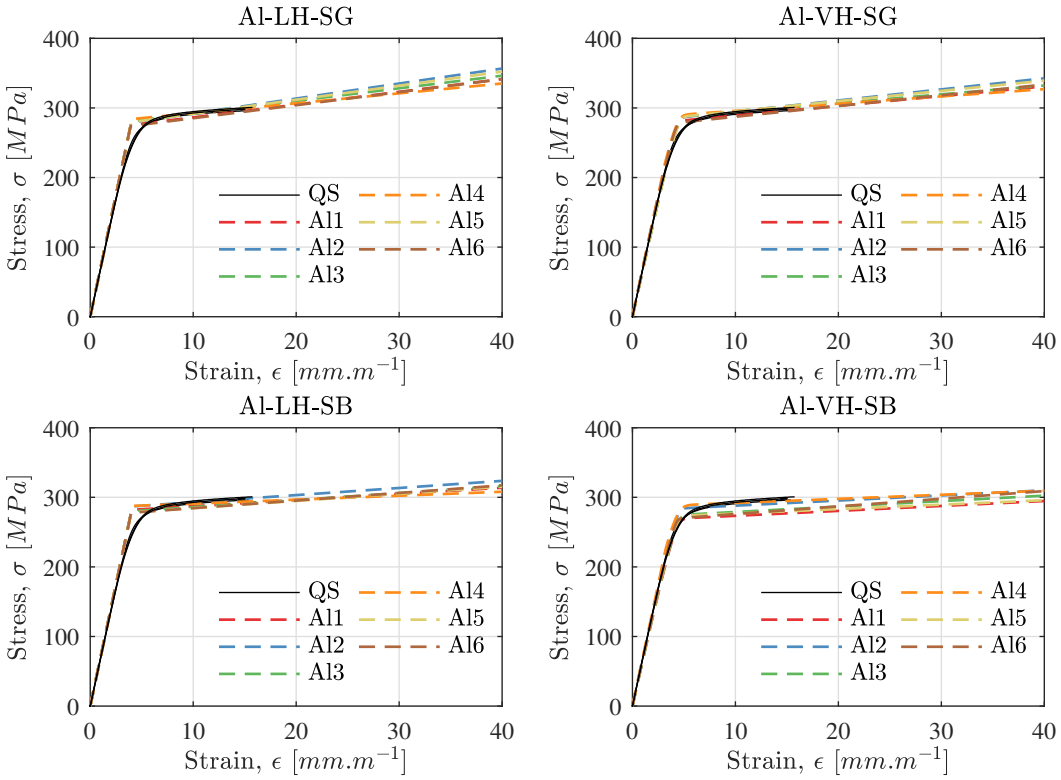

Figure 7: Comparison of quasi-static stress strain curves (raw data) and identified response for the dynamic tests.

variation between the three specimens. For the linear hardening case we observed that the SG virtuaal field gives a reasonable value for the initial yield stress while slightly overshooting the hardening modulus whereas the SB virtual fields slightly under-predict the initial yield stress while more accurately capturing the hardening modulus. A similar trend is observed for the Voce model where the under-prediction of the effective yield stress is more pronounced for the SB virtual fields. Comparison of the identified curves for the Voce model also show that the curvature of non-linear transition region is less defined than for the quasi-static case regardless of identification method.

Overall, the results in Figure 7 show that there is excellent agreement between the measured quasi-static response and the identified models from the dynamic tests. Given that the aluminium 6082-T6 considered here is not rate sensitive this provides the first experimental validation for applying the IBII methodology for elasto-plastic identification. Next we consider the same analysis for the stainless 316L samples where we expect a rate sensitive response.

4.3 Dynamic Identification: Steel

The results for all steel IBII samples are shown in Table 6. When considering the linear hardening case we see that the SG virtual field gives a higher initial yield stress but lower hardening modulus than the SB virtual fields. This contrasts with the aluminium results where the initial yield stress was consistent between methods and the hardening modulus was higher for the SG virtual field. The same trend is observed for the Voce model identified using the data from the steel specimens with a lower effective yield stress a and higher long term hardening modulus when the identification is performed with the SB virtual fields. However, given the scatter in the long term hardening modulus identified for the Voce model it is uncertain if this difference

	Linear				Voce						
SG	σ_0 $[MPa]$	H $[MPa]$	$max(\epsilon_p)$ [%]	$\hat{\dot{\epsilon}_p}$ $[s^{-1}]$	σ_0 $[MPa]$	R_0 $[MPa]$	R_{inf} $[MPa]$	b $[-]$	σ_{YS} $[MPa]$	$max(\epsilon_p)$ [%]	$\hat{\dot{\epsilon}_p}$ $[s^{-1}]$
St1	418	6137	4.06	2312	366	3294	82	698	448	3.82	2322
St2	424	5284	4.54	2259	196	5243	220	9.9×10^6	416	4.47	2387
St3	423	6858	3.75	1501	389	4638	64	632	452	3.71	1633
St4	420	7092	4.61	1629	389	3970	72	703	461	4.47	1754
St5	418	5171	4.00	2211	370	3357	71	725	441	3.85	2264
St6	434	4107	5.52	1946	254	4529	176	9.8×10^6	429	5.43	2080
Median	421	5711	4.30	2079	-	4249	-	714	445	4.16	2172
MAD	3.1	843	0.31	207	-	641	-	49	11.5	0.33	183
COV %	0.7	14.8	7.1	10.0	-	15.1	-	6.8	2.6	7.8	8.4
SB	σ_0 $[MPa]$	H $[MPa]$	$max(\epsilon_p)$ [%]	$\hat{\dot{\epsilon}_p}$ $[s^{-1}]$	σ_0 $[MPa]$	R_0 $[MPa]$	R_{inf} $[MPa]$	b $[-]$	σ_{YS} $[MPa]$	$max(\epsilon_p)$ [%]	$\hat{\dot{\epsilon}_p}$ $[s^{-1}]$
St1	391	8364	3.35	1746	248	6414	161	3316	408	3.28	1722
St2	418	6212	3.94	1844	280	4241	154	1808	435	3.93	1835
St3	400	8927	3.31	1282	353	5731	87	1234	440	3.29	1331
St4	402	7506	3.95	1402	303	6459	113	2452	416	3.84	1409
St5	402	7383	3.47	1783	108	4371	294	3653	402	3.47	1706
St6	405	6991	4.40	1505	323	3830	119	1257	442	4.40	1539
Median	402	7444	3.71	1626	-	5051	-	2130	425	3.65	1622
MAD	2.6	687	0.30	188	-	1016	-	885	15.8	0.32	156
COV %	0.7	9.2	8.1	11.5	-	20.1	-	41.5	3.7	8.7	9.6

Table 6: Identified elasto-plastic parameters from the dynamic tests on stainless steel 316L samples. Note that the coefficient of variation (COV) is taken as the ratio of the median absolute deviation (MAD) to the median.

is significant. The curvature parameter for the Voce model, b, is quite different for each method with the SG virtual field tending to give values around $600 - 700$ whereas the SB virtual fields give values above 1000. Also, two samples for SG virtual field return large values for b which effectively reduces the Voce model to be the same as the linear hardening case. This result suggests that the SB virtual fields give an improved consistency when identifying the curvature parameter b. This result is due to SB virtual fields creating tailored virtual fields to highlight areas where the b parameter is activated whereas the SG virtual field only accounts for the difference in average stress over a series of sample cross sections which may not be particularly sensitive to the b parameter.

The main interest for the steel data is comparison to the quasi-static response to observe the strain rate sensitivity as shown in Figure 8. All cases shown in Figure 8 exhibit an increase in initial yield stress and subsequent hardening behaviour compared to the quasi-static response. Here it is more difficult to determine which identification procedure produces the most accurate response because the underlying material behaviour is not known and the quasi-static data does not provide an absolute reference. Additionally, the hardening laws selected here are an approximation of the true material physics. Combining this uncertainty with the complex filtering process of full-field measurements and subsequent inverse identification it is not surprising that there are differences in the results. Despite the uncertainty about the underlying material model it is encouraging that all identification procedures are reasonably consistent in terms of the overall magnitude of the change in initial yield stress and subsequent hardening behaviour.

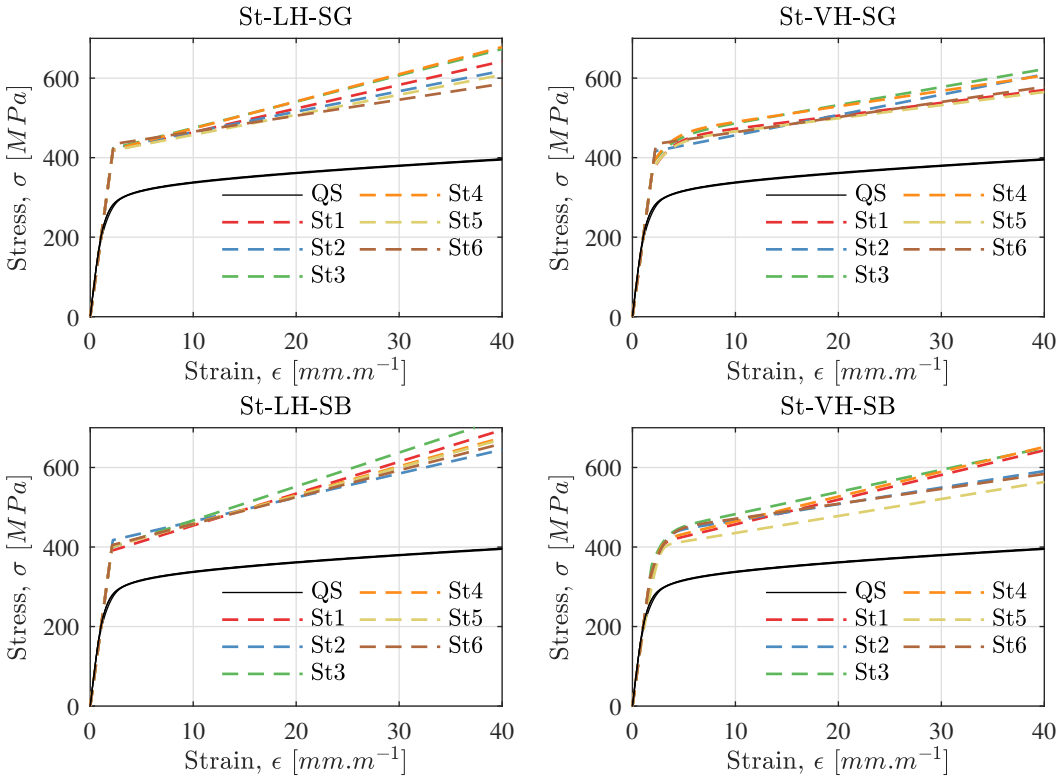

Figure 8: Comparison of quasi-static stress strain curves (raw data) and identified response for the dynamic tests.

Finally, we now compare our results to the rate sensitivity data for stainless steel 316L in the literature by revisiting Figure 1. This comparison is shown in Figure 9. In this figure the data from this study was reconstructed from the median response of the six tested samples given in Table 6 for the Voce hardening law. Interestingly, the results from this study most closely matches that obtained in [5] apart from the area close to the initial yield point. Some of this mismatch may results from the different hardening laws used but this does not explain the significant different between all cases given in Figure 9. It should also be noted here that it is difficult to directly compare the data from this study as the strain rate in the IBII test is heterogeneous. However, given that an order of magnitude change in strain rate is required to significantly alter the overall response of the Johnson-Cook models calibrated with the SHB data the comparison is reasonable.

5 Comparison with Image Deformation Simulations

For all results presented in the previous section the optimal processing parameters were used based on the synthetic image deformation study performed in part 1. The obvious follow up question is 'How well do the image deformation simulations match the experimental data?'. Therefore, the purpose of this section is to perform a comparison of the synthetic image deformation simulations to the experimental data. This was achieved by performing the same parameter sweep of spatial and temporal smoothing kernels as presented in part 1 for all experimental specimens. To make the image deformation simulations comparable to the experimental case the simulated images were polluted with a single copy of noise (rather than averaging over 30 copies of noise as in part 1) and the same smoothing parameter sweep was performed. All

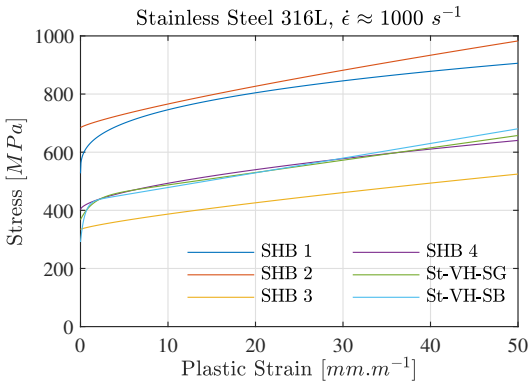

Figure 9: Comparison of the identified plastic response of stainless steel 316L from this study with data obtained using the using the SHB method. The SHB data is taken from the following references: SHB 1 [3]; SHB 2 [6]; SHB 3 [7] and; SHB 4 [5].

experimental specimens were collapsed to a single map for each identified parameter using the median over all six tests.

Here we focus on the aluminium data as the resulting material parameters are rate insensitive and should compare reasonably well to the quasi-static properties which were used as input to the image deformation model. The parameter maps comparing the experimental data to the synthetic image deformation are given in Figure 10 for the linear hardening case. These maps show an excellent agreement between the identified initial yield stress when the identification is performed using either using the SG or the SB virtual fields. The comparison is still remarkably good for the hardening modulus identified with the SG virtual field. The hardening modulus identified with the SB virtual fields is lower than that originally input into the image deformation model but the plateau region of stable identification above $S_{ks} = 21$ and $T_{ks} = 11$ is well captured. Overall, the comparison between the experimental and image deformation data is excellent for the linear hardening case providing confidence that the processing parameters selected using the image deformation simulations are appropriate.

Now we consider the same comparison for the Voce model as shown in Figure 11. Here we observed similar trends to the linear hardening model with excellent agreement for the effective yield stress. The comparison for the long term hardening modulus R_0, shows that the experimental data gives a lower long term hardening modulus regardless of identification method. However, the plateau region in the top right hand corner of the map (above $S_{ks} = 21$ and $T_{ks} = 11$) which returns a relatively stable value for R_0 is well captured by the image deformation simulations. For the curvature parameter b the comparison shows that the image deformation simulations accurately capture the region where the b parameter tends towards infinity when the identification is performed with the SG virtual field whereas the image deformation simulations predict that the SB virtual fields should be more stable which is in line with the experimental data.

Finally, we consider the error bounds predicted by the image deformation simulations performed in part 1 and the variability between experimental specimens given in Table 5. Table 7 gives a comparison between the coefficient of variation (COV) observed from the experimental data and that predicted by the image deformation simulations. This data shows that generally the predicted random error is within a factor of 2 to 4 of the experimental variability. The notable outlier is the predicted random error for the yield stress of the linear hardening model identified with the SG virtual field. It is currently unclear why a such a large difference occurs for this particular case. Overall, the results compare well to previous work analysing the errors

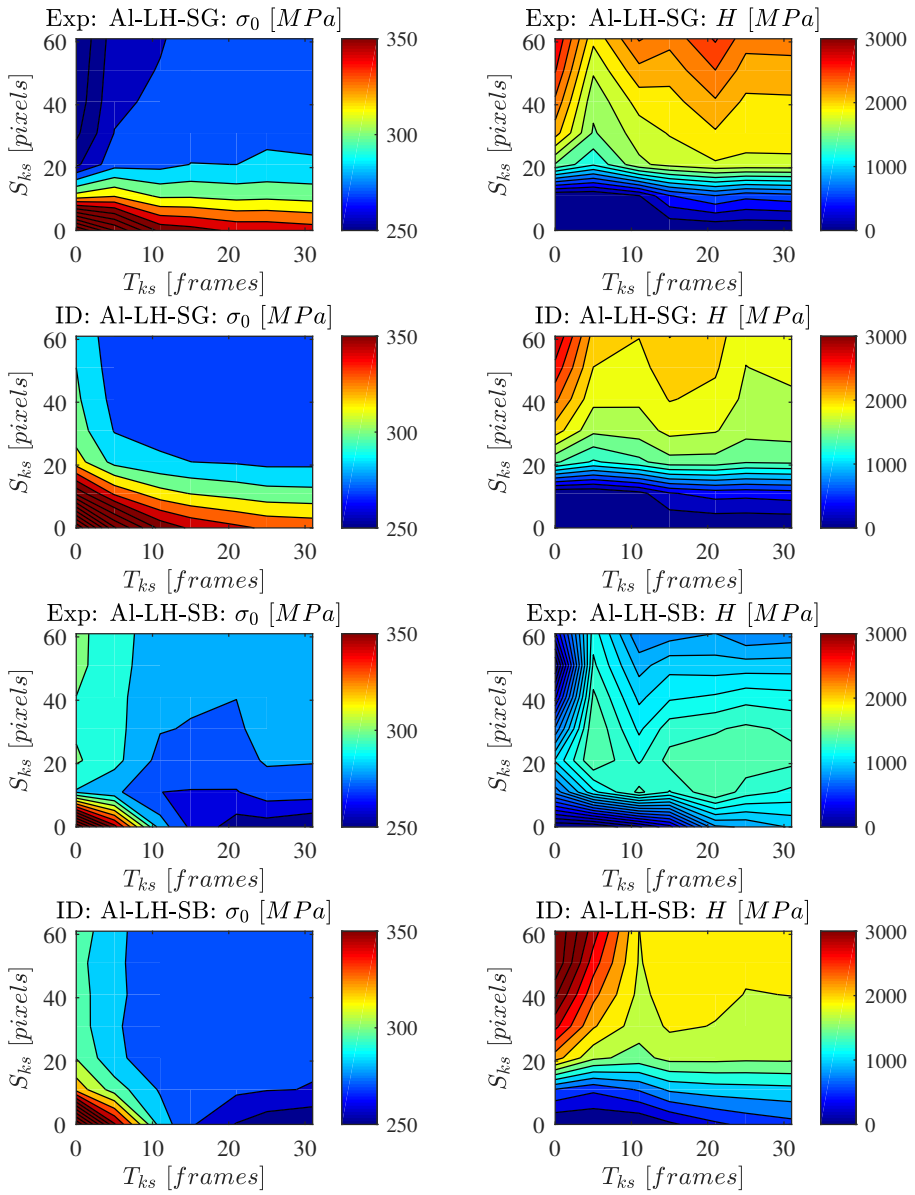

Figure 10: Comparison between the image deformation (ID) simulations and experimental (Exp) data for the identified material parameters of the linear hardening (LH) model. Note that the experimental data is the median of the identified parameters from all six tested samples.

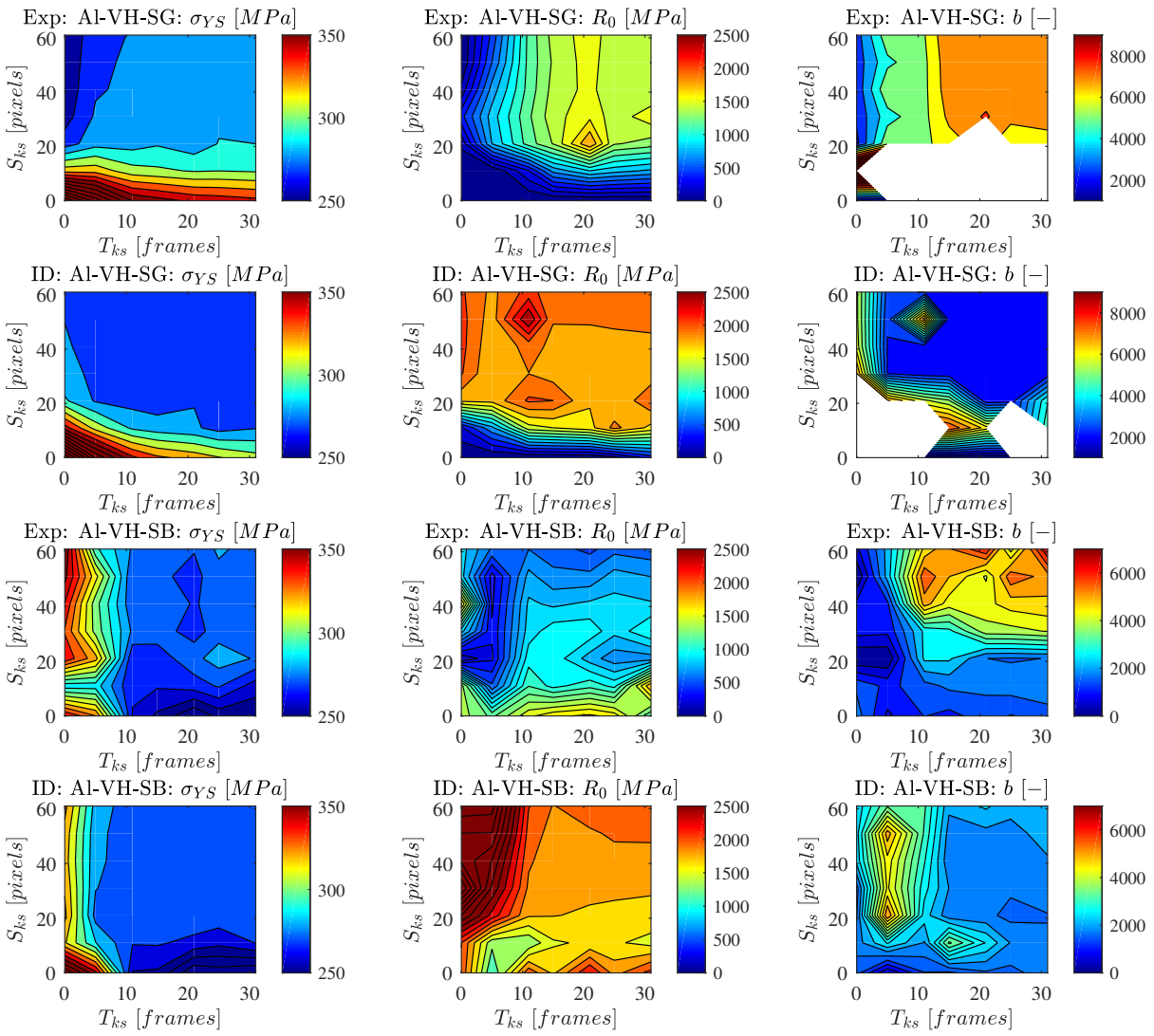

Figure 11: Comparison between image deformation (ID) simulations and experimental (Exp) data for the identified material parameters of the Voce model. Note that the experimental data is the median of the identified parameters from all six tested samples.

Al-SG	**Linear**		**Voce**		
COV [%]	σ_0	H	σ_{YS}	R_0	b
Exp.	1.03	5.64	0.78	9.68	7.98
ID	0.14	1.48	0.22	2.32	3.47
Al-SB	**Linear**		**Voce**		
COV [%]	σ_0	H	σ_{YS}	R_0	b
Exp.	1.04	4.47	1.61	10.1	21.7
ID	0.38	3.52	0.54	2.46	9.88

Table 7: Comparison of the coefficient of variation (COV) for the identified model parameter between experimental (Exp) and simulated image deformation (ID) data.

for the orthotropic elastic constants of foams as described in [23] where the experimental standard deviation was approximately double that predicted by the image deformation simulations. Here the problem is more challenging than in elasticity as the tests are destructive and it is not possible to repeat measurements on a single sample to analyse variability. Despite this it is encouraging that the image deformation simulations predict an error that is reasonably close to that obtained experimentally.

Obviously, some of the variability over the tested specimens can be attributed to material variability but given that the quasi-static curves shown in Figure 7 and 8 are indistinguishable from one another the material variability can be assumed to be low. There are many factors which are not captured by the image deformation simulations which can cause the differences observed between the experimental data and image deformation simulations. This is evident when considering the underlying assumptions of the image deformation analysis. In an experiment the noise is grey level dependent, the lighting is non-uniform and the grids have defects. All of these factors are not captured by the analytic grid deformation procedure despite the overall measurement resolution being similar (see Table 3). It would be possible to deform real experimental grid images using a sub-pixel interpolation method as described in [22, 33] which would capture some of the aforementioned errors. In the future it would be interesting to perform this study to determine how much of the difference in variability can be accounted by sequentially increasing the factors which are considered by the synthetic image deformation procedure.

The last factor that affects the comparison between the experimental data and the image deformation simulations is the difference between the chosen constitutive model and the true unknown material physics. The material model identified from the experiment is only a best fit of the given model to the experimental data so the preceding analysis does not account for the unknown material model error. Choosing the most suitable material model for any given problem is still an open problem and there is considerable work to be undertaken in this field.

6 Limitations and Future Work

The results of numerical analysis and experimental validation presented in this study have shown that the IBII methodology can be used for the identification of elasto-plastic behaviour under high strain rate loading. However, there are several limitations which need to be discussed to determine the scope of the present results:

3D Effects: a key assumption that is used to analyse IBII test data using the VFM is that the kinematic fields must be uniform through the thickness of the sample such that the volume integrals collapse to 2D. The validity of this assumption was analysed experimentally in ref.

[34] for the case of elastic modulus identification and tensile failure stress identification for a quasi-brittle material. In this study it was found that a bending wave created by projectile misalignment lead to small bias on the elastic modulus but a significant bias on the tensile failure stress. As a result, the alignment procedure was updated and significantly better results were obtained.

The experimental data presented in this study was obtained before the work in [34]. Therefore, it is possible that the presence of 3D loading explains some of the differences observed between test samples as well as the increase in scatter between the quasi-static and dynamic test data. Analysis of the exact errors induced by 3D loading for elasto-plasticity would require a similar systematic study with back-to-back imaging as presented in [34].

As this is only the first development of an elasto-plasticity identification procedure using the IBII test method there are several key areas for future work which are discussed below:

Visco-Plasticity: the focus of the present work was the identification of initial yield and hardening law parameters whereas in refs. [17, 18] the focus was on identifying rate sensitivity parameter with yield and hardening parameters taken from quasi-static test data. Given that the IBII test includes heterogeneous strain rate information it would seem logical to combine these two approaches. This must be approached with some caution as the loading in the IBII test occurs over an extremely short period, on the order of micro-seconds, which is not a sufficient amount of time for long term plasticity/dissipation mechanisms to react. Therefore, the predicted results with the IBII test using the instantaneous strain rate might not be able to be extrapolated back to the quasi-static response. How best to use the information obtained in the IBII test is still an open question for visco-plasticity and visco-elasticity.

Anisotropic Plasticity: the accurate prediction of sheet metal forming processes requires knowledge of anisotropic response of metals under high strain rate loading. It was recently shown that the SB virtual fields can be used for the identification of anisotropic plasticity models under quasi-static loading in [35, 36]. This makes the SB virtual fields an ideal method for the identification of anisotropic plasticity at high strain rate. To activate all of the model parameters it will be necessary to use tests at different angles and/or tests with for complex geometry. The use of geometric features such as holes and notches induces further problems with missing data at edges. However, future advances in ultra-high speed camera technology leading to larger pixel arrays will mitigate this problem.

Heterogeneous Plasticity: Welding is a common joining technique that produces heterogenous material properties. In order to predict failure of welded structures under impact loading it is necessary to understand the dynamic response the heterogenous material in the weld zone. A first attempt at using inverse identification to analyse friction stir welds was made in [37]. However, there has been minimal additional work since, despite the advancements in camera technology. The main challenge for heterogeneous material properties is similar to the above discussion for anisotropic plasticity in that higher spatial resolution cameras are required to spatially resolve the material response.

Extension to 3D for Large Strains: a significant challenge when analysing the large strain plastic behaviour of metals is the strong heterogeneity through the sample thickness when large strains occur (commonly referred to as necking). It was recently shown that stereo DIC measurements could be used for 3D reconstruction of kinematics for large strain metal plasticity [33]. This method could also be applied to an IBII-like configuration removing the assumption that the test is 2D and allowing the volume integrals in the principle of virtual work to be evaluated.

This idea is similar to creating an instrumented Taylor impact test where stereo DIC is used with the procedure in [33]. The development of this new method would require a thorough validation using finite element modelling coupled with synthetic image deformation simulations for stereo DIC.

7 Conclusion

This study is the second in a two part series describing the development of a new high strain rate elasto-plastic identification procedure using the IBII test method. Here two identification methods were analysed including the use of the stress-gauge (SG) virtual field and the recently developed sensitivity-based (SB) virtual fields. The present work focused on the experimental validation of the method. The key results are summarised as follows:

1. The identification results for the rate insensitive aluminium 6082-T6 samples showed excellent consistency between quasi-static and dynamic test results, thus providing an experimental validation of the method.

2. The identification results for the rate sensitive steel 316L samples showed increases in yield stress and hardening behaviour compared to quasi-static tests.

3. Identifications performed with the stress-gauge (SG) virtual field and the sensitivity-based (SB) virtual fields were consistent across all cases with the SB virtual fields leading to a more stable identification of the curvature parameter of the Voce hardening model.

4. The experimental variability was higher than that predicted by the image deformation simulations by a factors of 2 to 4, indicating that present image deformation methodology accounts for approximately half to a quarter of the observed experimental variability (not accounting for material model error).

5. Comparison of the experimental data with the image deformation simulations showed good agreement based on a sensitivity sweep of smoothing parameters used to process the data especially for the yield stress parameters of both the linear and Voce models.

This study demonstrates the first application of the IBII method to identify a non-linear material model in the form of the elasto-plastic response of metals. There are many avenues for future development of the IBII method related to non-linear material model identification but the logical next step is to combine the method presented here with that in [17, 18] to identify plasticity parameters and rate sensitivity parameters in a single test. The development of these new IBII tests will reduce the number of tests that are required to characterise a given material by using heterogeneity in strain rate that is inherent to the IBII test configuration. Ultra-high speed camera technology will only improve in the future providing improved accuracy for the identification method presented in this work. An increase in spatial resolution is especially important here as the majority of the plastic strain is concentrated at the impact edge of the sample where data is lost due to edge effects. Furthermore, increases in spatial resolution will allow for the use of geometrical features such as holes or notches further increasing the heterogeneity of the test and providing more detailed information for model identification.

Acknowledgements

The authors would like to thank Prof. Clive Siviour from the University of Oxford who helped with preliminary experiments that aided in establishing the experimental method detailed in

this work. Prof. Pierron and Dr Dreuilhe acknowledge support from US Air Force / EOARD (grant FA8655-13-1-3041). The authors are grateful to the program manager, Dr Matt Snyder, for supporting this work. Dr Frances Davis, Dr Lloyd Fletcher and Prof. Fabrice Pierron acknowledge support from EPSRC through grant EP/L026910/1.

This material is based on research sponsored by the Air Force Research Laboratory, under agreement number FA8655-13-1-3041. The U.S. Government is authorized to reproduce and distribute reprints for Governmental purposes notwithstanding any copyright notation thereon. The views and conclusions contained herein are those of the authors and should not be interpreted as necessarily representing the official policies or endorsements, either expressed or implied, of the Air Force Research Laboratory or the U.S. Government.

Data Provision

All data supporting this study are openly available from the University of Southampton repository at: http://dx.doi.org/10.5258/SOTON/xxxxx. The digital dataset contains the following:

1. Static reference images and measurement resolution analysis Matlab code.
2. Dynamic test images for all samples and the calculated kinematic fields for each optimal combination of smoothing parameters.
3. Matlab code for performing the elasto-plastic identification and smoothing sensitivity analysis.
4. Smoothing sensitivity maps for the identified material parameters for all experimental samples.

References

[1] J. E. Field, S. M. Walley, W. G. Proud, H. T. Goldrein, and C. R. Siviour. Review of experimental techniques for high rate deformation and shock studies. *International Journal of Impact Engineering*, 30(7):725–775, August 2004.

[2] B. A. Gama, S. L. Lopatnikov, and J. W. Gillespie. Hopkinson bar experimental technique: a critical review. *Applied Mechanics Reviews*, 57(4):223–250, October 2004.

[3] W.-S. Lee, C.-F. Lin, T.-H. Chen, and W.-Z. Luo. High temperature deformation and fracture behaviour of 316L stainless steel under high strain rate loading. *Journal of Nuclear Materials*, 420(1):226–234, January 2012.

[4] D. Umbrello, R. M'Saoubi, and J. C. Outeiro. The influence of Johnson–Cook material constants on finite element simulation of machining of AISI 316L steel. *International Journal of Machine Tools and Manufacture*, 47(3):462–470, March 2007.

[5] H. Chandrasekaran, R. M'Saoubi, and H. Chazal. Modelling of material flow stress in chip formation process from orthogonal milling and split Hopkinson bar tests. *Machining Science and Technology*, 9(1):131–145, March 2005.

[6] Rachid Msaoubi. *Aspects thermiques et microstructuraux de la coupe. Application a la coupe orthogonale des aciers austenitiques.* thesis, Paris, ENSAM, January 1998.

[7] B. Changeux, M. Touratier, J.L. Lebrun, T. Thomas, and J. Clisson. High-speed shear tests for the identification of the Johnson–Cook law. In *Fourth International ESAFORM Conference*, pages 603–606, Liège, Belgium, April 2001.

[8] F. Pierron and P. Forquin. Ultra-high-speed full-field deformation measurements on concrete spalling specimens and stiffness identification with the virtual fields method. *Strain*, 48(5):388–405, October 2012.

[9] F. Pierron, H. Zhu, and C. Siviour. Beyond Hopkinson's bar. *Philosophical Transactions of the Royal Society of London A: Mathematical, Physical and Engineering Sciences*, 372(2023), August 2014.

[10] R. Seghir and F. Pierron. A novel image-based ultrasonic test to map material mechanical properties at high strain-rates. *Experimental Mechanics*, 58(2):183–206, February 2018.

[11] J. Van Blitterswyk, L. Fletcher, and F. Pierron. Image-based inertial impact test for composite interlaminar tensile properties. *Journal of Dynamic Behavior of Materials*, 4(4):543–572, December 2018.

[12] L. Fletcher and F. Pierron. An image-based inertial impact (IBII) test for tungsten carbide cermets. *Journal of Dynamic Behavior of Materials*, 4(4):481–504, December 2018.

[13] P. Forquin, B. Lukić, D. Saletti, L. Sallier, and F. Pierron. A benchmark testing technique to characterize the stress–strain relationship in materials based on the spalling test and a photomechanical method. *Measurement Science and Technology*, 30(12):125006, September 2019.

[14] L. Fletcher and F. Pierron. The image-based inertial release (IBIR) test: a new high strain rate test for stiffness strain-rate sensitivity identification. *Experimental Mechanics*, 60(4):493–508, April 2020.

[15] L. Fletcher, J. Van-Blitterswyk, and F. Pierron. Combined shear/tension testing of fibre composites at high strain rates using an image-based inertial impact test. In *EPJ Web of Conferences*, volume 183, page 02041, 2018.

[16] L. Fletcher, J. Van-Blitterswyk, and F. Pierron. A novel image-based inertial impact test (IBII) for the transverse properties of composites at high strain rates. *Journal of Dynamic Behavior of Materials*, 5(1):65–92, March 2019.

[17] P. Bouda, B. Langrand, D. Notta-Cuvier, E. Markiewicz, and F. Pierron. A computational approach to design new tests for viscoplasticity characterization at high strain-rates. *Computational Mechanics*, June 2019.

[18] T. Fourest, P. Bouda, L. C. Fletcher, D. Notta-Cuvier, E. Markiewicz, F. Pierron, and B. Langrand. Image-based inertial impact test for characterisation of strain rate dependency of Ti6Al4V titanium alloy. *Experimental Mechanics*, 60(2):235–248, February 2020.

[19] L. Fletcher, F. Davis, S. Dreuilhe, A. Marek, and F. Pierron. High strain rate elasto-plasticity identification using the image-based inertial impact (IBII) test part 1: error quantification. *Strain*, 2020. Under review.

[20] P. Lava, S. Cooreman, S. Coppieters, M. De Strycker, and D. Debruyne. Assessment of measuring errors in DIC using deformation fields generated by plastic FEA. *Optics and Lasers in Engineering*, 47(7–8):747–753, July 2009.

[21] P. Lava, S. Cooreman, and D. Debruyne. Study of systematic errors in strain fields obtained via DIC using heterogeneous deformation generated by plastic FEA. *Optics and Lasers in Engineering*, 48(4):457–468, April 2010.

[22] M. Rossi, P. Lava, F. Pierron, D. Debruyne, and M. Sasso. Effect of DIC spatial resolution, noise and interpolation error on identification results with the VFM. *Strain*, 51(3):206–222, June 2015.

[23] P. Wang, F. Pierron, M. Rossi, P. Lava, and O. T. Thomsen. Optimised experimental characterisation of polymeric foam material using DIC and the virtual fields method. *Strain*, 52(1):59–79, 2015.

[24] B. Lukić, D. Saletti, and P. Forquin. Use of simulated experiments for material characterization of brittle materials subjected to high strain rate dynamic tension. *Phil. Trans. R. Soc. A*, 375(2085):20160168, January 2017.

[25] W. Moćko, J. A. Rodríguez-Martínez, Z. L. Kowalewski, and A. Rusinek. Compressive viscoplastic response of 6082-T6 and 7075-T6 aluminium alloys under wide range of strain rate at room temperature: experiments and modelling. *Strain*, 48(6):498–509, 2012.

[26] P. Yibo, W. Gang, Z. Tianxing, P. Shangfeng, and R. Yiming. Dynamic mechanical behaviors of 6082-T6 aluminum alloy. *Advances in Mechanical Engineering*, 5:878016, January 2013.

[27] X. Chen, Y. Peng, S. Peng, S. Yao, C. Chen, and P. Xu. Flow and fracture behavior of aluminum alloy 6082-T6 at different tensile strain rates and triaxialities. *PLOS ONE*, 12(7):e0181983, July 2017.

[28] A. Marek, F. M. Davis, and F. Pierron. Sensitivity-based virtual fields for the non-linear virtual fields method. *Computational Mechanics*, 60(3):409–431, September 2017.

[29] L. Fletcher, J. Van Blitterswyk, and F. Pierron. A manual for conducting image-based inertial impact (IBII) tests, August 2019. http://dx.doi.org/10.5258/SOTON/P0015.

[30] M. Grédiac, B. Blaysat, and F. Sur. A critical comparison of some metrological parameters characterizing local digital image correlation and grid method. *Experimental Mechanics*, 57(6):871–903, July 2017.

[31] M. Grédiac, F. Sur, and B. Blaysat. The grid method for in-plane displacement and strain measurement: a review and analysis. *Strain*, 52(3):205–243, June 2016.

[32] E. A. de Souza Neto, D. Peric, and D. R. J. Owen. *Computational methods for plasticity: theory and applications*. John Wiley & Sons, September 2011.

[33] M. Rossi, L. Cortese, K. Genovese, A. Lattanzi, F. Nalli, and F. Pierron. Evaluation of volume deformation from surface DIC measurement. *Experimental Mechanics*, 58(7):1181–1194, September 2018.

[34] J. Van Blitterswyk, L. Fletcher, and F. Pierron. Investigation of the 2D assumption in the IBII test. *Strain*, 2020. Under review.

[35] A. Marek, F. M. Davis, M. Rossi, and F. Pierron. Extension of the sensitivity-based virtual fields to large deformation anisotropic plasticity. *International Journal of Material Forming*, 12(3):457–476, May 2019.

[36] A. Marek, F. M. Davis, J.-H. Kim, and F. Pierron. Experimental validation of the sensitivity-based virtual fields for identification of anisotropic plasticity models. *Experimental Mechanics*, 60(5):639–664, June 2020.

[37] G. Le Louëdec, F. Pierron, M. A. Sutton, C. Siviour, and A. P. Reynolds. Identification of the Dynamic Properties of Al 5456 FSW Welds Using the Virtual Fields Method. *Journal of Dynamic Behavior of Materials*, 1(2):176–190, March 2015.